Reinforcement learning based plasma flow control of asymmetric vortices over a slender body at high angles of attack

Borui Zheng (郑博睿)[1,2,3*], Peng Gao(高鹏)[1,2,3], Haodong Liu(刘浩东)[4], Yichi Liu(刘毅驰)[1,2,3],

Shuaimin An (安帅民) [1,2,3], Yilun Wei (魏逸伦) [1,2,3], Jiayin Chen (陈嘉印) [1,2,3], Fengqing Liu(刘凤庆) [1,2,3],

Hongwei Wu(吴宏伟)[5], Bangdou Huang(黄邦斗)[6], Minghao Yu(喻明浩)[4], Chang Ge(葛畅)[7,8]

[1]School of Automation and Information Engineering, Xi’an University of Technology, Xi’an 710048, China

[2]Shaanxi Key Laboratory of Complex System Control and Intelligent Information Processing, Xi'an 710048, China

[3]Shaanxi University Key Laboratory of Photonic Power Devices and Discharge Regulation, Xi'an 710048, China

[4]School of Mechanical and Precision Instrument Engineering, Xi'an University of Technology, Xi'an 710048, China

[5]School of Physic, Engineering and Computer Science, University of Hertfordshire, Hatfield AL10 9AB, United Kingdom

[6]Institute of Electrical Engineering, Chinese Academy of Sciences, Beijing 100190, China

[7]School of Art and Design, Xi'an University of Technology, Xi’an 710048, China

[8]College of Engineering, Design and Physical Sciences, Brunel University London, London, UB 8 3PH, United Kingdom

*E-mail of the corresponding author: narcker@xaut.edu.cn

Abstract: Slender-body aircraft operating at high angles of attack often experience nonlinear, asymmetric multi-vortex flow structures that generate random, unsteady lateral forces, undermining stability and maneuverability. Dielectric barrier discharge plasma actuators can eliminate these lateral forces. However, conventional open-loop plasma control method cannot adapt to dynamic flow fields in real time, limiting the overall effectiveness of active flow control. This study introduces a plasma control framework grounded in physical principles and develops plasma actuator design methods to regulate vortex interactions, stabilize flow dynamics, and optimize control efficiency. An intelligent closed-loop flow control strategy based on Proximal Policy Optimization, a deep reinforcement learning algorithm, is utilized to enable real-time plasma parameter adjustments for suppressing lateral force at high angle of attack. The spatiotemporal interaction of plasma-induced and asymmetric vortices was investigated through synchronized pressure measurements and particle image velocimetry. The Proximal Policy Optimization based parameter optimization model was trained online in an educational open-return wind tunnel and subsequently deployed in a low-speed closed-return wind tunnel. Based on vortex stability analysis and comprehensive results, the closed-loop control algorithm, significantly mitigates lateral forces, achieving a 68.5% reduction compared to steady plasma actuation, while improving energy efficiency by 70% over conventional methods.

I. Introduction

The forebodies of modern high-performance airplanes and missiles are usually designed with a slender revolution/axisymmetric shape (e.g., a cone) to reduce aerodynamic drag. To attain superior maneuverability, these aircraft must perform effectively at high angles of attack (AOA) or even post-stall. However, when such a slender aircraft maneuvers at a high AOA under zero sideslip conditions, the surrounding flow field often exhibits complex multi-vortex structures, with the aerodynamic parameters undergoing rapid, unsteady, and nonlinear change, eventually leading to random lateral forces and yaw moments [1-2]. Under these conditions, the conventional control surfaces, such as vertical and horizontal tails, are submerged in turbulent wakes, making them incapable of providing the required control. Once the sideslip phenomenon occurs, the aircraft may quickly experience complex and unpredictable tailspin, wing rock, wing drop, and nose slice, significantly impairing its flight performance and leading to catastrophic loss.

The random lateral forces are caused by forebody asymmetric vortices (FAV) forming in the leeward region along the slender aircraft's fuselage. The directions and magnitudes of the lateral forces are determined by these asymmetric vortices, which have different strengths and spatial distributions [3-4]. Therefore, Effective flow control methods are urgently needed to suppress the formation and development of forebody asymmetric vortices, thereby suppressing lateral forces and yaw moments. These advancements will enhance aircraft stability and maneuverability during high AOA flight.

The key to controlling forebody asymmetric vortices over a slender aircraft lies in modulating their vorticity strength and spatial distribution [4], thereby generating yaw control moments that can compensate for or even replace the lost effectiveness of traditional control surfaces. Minor perturbations near the apex can significantly influence the flow pattern over the slender body [5]. This sensitivity enables compact control devices installed on the aircraft’s forebody, which require minimal space and weight compared to traditional control surfaces. Additionally, the longer moment arms provided by slender forebodies amplify the lateral forces, allowing significant yaw control moments to be achieved with minimal energy input. This is a practical example of active flow control' s “smaller input, larger output” principle. Furthermore, forebody vortex control techniques offer additional benefits, such as reducing the weight of traditional control surfaces and minimizing radar cross-sections.

Forebody vortex control methods can be categorized into passive and active control based on external energy input requirements [6]. Passive control methods modify the flow field by geometric changes or the addition of mechanical devices. These methods are characterized by structural simplicity and without external energy input. However, once fixed, the geometry structure or mechanical devices are difficult to adjust, limiting their effectiveness to specific flow states. Under other conditions, their control efficiency often diminishes and may even lead to adverse effects. Typical passive control techniques include strakes, micro-bumps, micro-dimples, grit strips, nose bluntness, vortex generators, and self-excited oscillating flags [7-11]. Active control methods, in contrast, require continuous energy input during operation. They provide significant control effects and adjustable actuation parameters, enabling optimized performance across various flow states. Despite their complexity, active control methods show promise for adaptive and intelligent flow control. Examples include plasma actuators, nose blowing, synthetic jets, and micro-balloon arrays [12-15].

Plasma actuators are electrical devices which can generate a near wall jet without any moving parts [16]. Research using plasma actuators to control forebody asymmetric vortices over a slender forebody began in 2004. Initially, arc discharge was employed to conical forebodies, which could change the separation position of the boundary layer and enable modulating of the asymmetric vortices [17]. However, due to the instability of the arc discharge and the resulting high temperatures will damage the experimental model, subsequent research shifted focus to dielectric barrier discharge (DBD). DBD plasma actuators can effectively control lateral forces on slender bodies, particularly through precise placement near the cone apex and duty-cycle modulation techniques (operates alternately with complementary duty ratios) [18]. Recent studies have further optimized actuator layouts and electrical parameters, enabling near-linear proportional control of lateral forces and yaw moments over a broader range of flow conditions (AOA 35°-55° and Re (10^5) [19-24]. Additionally, closed-loop control systems and feedback mechanisms have significantly improved the accuracy and adaptability of plasma actuation, marking a notable advancement in intelligent vortex control technology [25-26].

Most existing asymmetric vortex control methods rely on open-loop control, which cannot adapt to real-time changes in the flow field. As flow velocity and AOA increase, the intensification of primary vortices and stronger interactions between vortex pairs ultimately lead to the failure of open-loop control. These limitations stem from three critical challenges: (1) Energy Efficiency Challenges: The low energy efficiency of DBD plasma actuators restricts their overall control performance and application applicability. (2) Mechanistic Uncertainty Limitations: The unclear mechanisms of plasma discharge's effects on key flow field parameters results in inadequate theoretical guidance for designing effective plasma control strategies. (3) Adaptive Control Deficiency: Current control methods cannot dynamically adjust control strategies and actuation parameters in real time, preventing the implementation of adaptive control systems for robust and efficient asymmetric vortex control.

This paper presents an intelligent plasma control method based on Proximal Policy Optimization (PPO) to modulate forebody asymmetric vortices over slender bodies at high AOA. Based on physical principles, three control strategies are proposed: regulating vortex interactions, stabilizing the flow field, and controlling velocity gradients. These strategies are translated into practical plasma actuator design principles (structural design, interference mitigation, and control optimization) forming a comprehensive framework to enhance flow field stability and control effectiveness. The PPO algorithm is trained, and plasma parameters are optimized in an educational open-return wind tunnel. Subsequently, the optimized parameters are deployed in a closed-return wind tunnel for further validation. The control effectiveness is evaluated through synchronized particle image velocimetry (PIV) and static pressure measurements, revealing significant insights into adaptive strategies for managing forebody asymmetric vortices under high-AOA conditions. This work provides insights into the dynamics of plasma-induced vortex control and highlights the potential of intelligent closed-loop plasma systems for improving control efficiency and extending the flight envelope of slender-body aircraft.

II. Control strategy analysis

The generation of forebody asymmetric vortices depends on the vortex stability conditions over a slender body at high AOA. External minor perturbations, such as plasma energy injection, can affect vortex stability conditions by altering local velocity gradients and vorticity distributions, thereby modifying the strength and spatial distribution of asymmetric vortices. Therefore, understanding the dynamic evolution of vortex structure under these perturbations is key to developing effective asymmetric vortex control strategies.

Based on the conical flow assumption, the three-dimensional flow problem can be reduced to a two-dimensional, steady, inviscid, incompressible, conical, and slender flow [5]. The flow is irrotational except at the center of the isolated vortices. By analyzing the eigenvalues of the dynamic equation governing vortex flow, the dynamic response and stability of vortex pairs under symmetric and asymmetric disturbances can be evaluated [27]. The flow around a slender body is characterized as absolute (temporal) stability, in which the growth or decay of minor perturbations is determined by the system's dynamic properties, independent of the spatial propagation of the minor perturbations. When the minor perturbations are applied and removed, whether the system can restore to its original state depends on the divergence and Jacobian of the vortex velocity field evaluated at the stationary points [28].

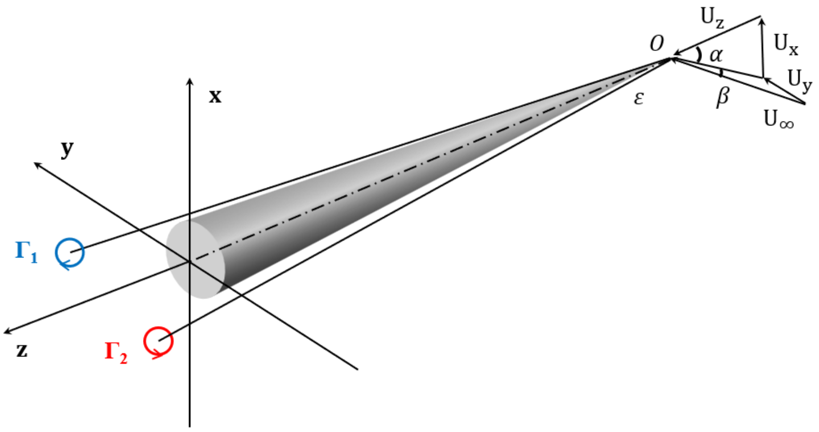

Figure 1 Slender conical body with coordinate system and symmetric separation vortices.

Consider the flow past a slender conical body at an angle of attack α and sideslip angle β (the effect of β is neglected in this study), with the rectilinear body coordinates (x, y, z), as shown in Figure 1. The freestream velocity is U_∞. Based on Equation (1), Cai et al. calculated the vortex velocity in the flow field and analyzed the stability of vortex pairs and the evolution of perturbations, thereby providing a theoretical basis for the effective control of asymmetric vortices over slender bodies at high AOA [5].

$$u - iv = U_\infty \times \left(1 - \frac{1}{\zeta^2}\right) + \frac{i\Gamma}{2\pi}\left[\frac{1}{\zeta - 1/\zeta} - \frac{1}{\zeta - \bar{\zeta}} - \frac{1}{\zeta - 1/\bar{\zeta}}\right] \tag{1}$$

In Equation (1), $u - iv$ represents the complex vortex velocity at any point in the flow field; u represents the real part of the vortex velocity (x-direction/horizontal component); v represents the imaginary part of the vortex velocity (y-direction/vertical component); U_∞ is the free-stream velocity; $U_\infty\left(1 - 1/\zeta^2\right)$ describing the flow field changes caused by the cylinder surface; ζ represents a position in the complex domain of the flow field, expressed as a complex number $\zeta = \xi + i\eta$, where ξ is the real part (x-coordinate) and η is the imaginary part (y-coordinate). Γ is the strength (circulation) of the vortex. ζ_0 is the complex position of the vortex core (main vortex), which can be found by removing the self-induced velocity term due to the vortex itself; $\overline{\zeta_0}$ is the conjugate position of the vortex core (mirror vortex position);

$1/\zeta^2$ reflects the cylinder's induced effect.

In the case of two-dimensional flow, assume that a vortex is located at a specific position (x, y) in the flow field and is subject to external minor perturbations. If the vortex position shifts slightly from its stationary position (x_0, y_0) due to the minor perturbations, the vortex velocity (u, v) can describe the vortex's motion. The stationary position, also referred to as a velocity stagnation point or stationary point, is defined as the location in the flow field where the vortex velocity components satisfy $u(x,y)=0$ and $v(x,y)=0$. By performing a Taylor expansion of the velocity field, the approximate equation of motion for the vortex position can be derived from Equation (2):

$$\frac{d}{dt}\begin{bmatrix}\Delta x\\ \Delta y\end{bmatrix}=\begin{bmatrix}u\\ v\end{bmatrix}=\begin{bmatrix}\left(\frac{\partial u}{\partial x}\right)_0 & \left(\frac{\partial u}{\partial y}\right)_0\\ \left(\frac{\partial v}{\partial x}\right)_0 & \left(\frac{\partial v}{\partial y}\right)_0\end{bmatrix}\begin{bmatrix}\Delta x\\ \Delta y\end{bmatrix} \tag{2}$$

Where $\Delta x = x - x_0$ and $\Delta y = y - y_0$ represent the small displacements of the vortex from its stationary point (x_0, y_0). These points are critical in stability analysis as they represent the equilibrium configuration of the vortex system, where external perturbations may cause deviations that determine the stability behavior. When the vortex is perturbed from its stationary point (x_0, y_0) and then released, its motion is assumed to follow the vortex velocity (u, v).

The Jacobian J of the vortex velocity field quantifies the local linearized deformation of the flow field, reflecting how perturbations evolve (growth or decay) in the vicinity of the stationary points. Specifically, it captures the coupling between velocity components in orthogonal directions. On the other hand, the divergence D of the vortex velocity field represents the volumetric expansion or contraction rate of the flow at a given point, and indicating whether the local fluid volume is increasing ($D > 0$)

or decreasing ($D < 0$). These metrics are critical in determining the stability of the vortex system under external minor perturbations.

$$J = \begin{vmatrix} \frac{\partial u}{\partial x} & \frac{\partial u}{\partial y} \\ \frac{\partial v}{\partial x} & \frac{\partial v}{\partial y} \end{vmatrix}, \quad D = \nabla \cdot q = \frac{\partial u}{\partial x} + \frac{\partial v}{\partial y} \tag{3}$$

By solving the eigenvalues of the vortex system, the stability conditions of the system can be determined. The eigenvalues of the coefficient matrix in Equation (2) represent the growth rates of perturbations in the vortex system.

$$\lambda_{1,2} = \frac{1}{2}\left(D_0 \pm \sqrt{D_0^{\;2} - 4J_0}\right) \tag{4}$$

Here D_0 and J_0 represent the divergence and Jacobian of the vortex velocity field at the stationary point. According to Equation (4), the stability of the vortex system is determined by the real part of these eigenvalues: if $\mathrm{Re}(\lambda) < 0$, disturbances decay, and the vortex system remains stable; if $\mathrm{Re}(\lambda) > 0$, disturbances grow, leading to instability. The condition for stability is met only when $D_0 < 0$ (indicating a contracting flow region) and $J_0 > 0$ (indicating a positive local deformation that resists divergence). This establishes a clear relationship between the flow field's local physical parameters and the overall stability of the vortex system. There is a causal relationship: flow field stability directly influences the symmetry of vortex pairs over a slender body at high AOA. A stable flow field suppresses the growth of disturbances, maintaining vortex pair symmetry and preventing asymmetric vortex formation. This study employs plasma control strategies to enhance vortex stability by modulating local velocity gradients and vorticity distributions.

Asymmetric vortex control strategies can be derived from the above equations. ① **Vortex interaction regulation**: According to Equation (1), reducing vortex circulation or increasing the distance between vortex pairs decreases the induced velocity, facilitating the balance of the asymmetric vortex spatial structure. ② **Flow Field Stability Optimization**: According to Equation (4), $D_0 < 0$ and $J_0 > 0$ must be satisfied to achieve a negative real part of the eigenvalue. To achieve $D_0 < 0$, the plasma jet strength and actuation frequency should be optimized to increase the local flow field and cause the fluid to contract. ③ **Velocity Gradient Control**: To achieve $J_0 > 0$, the plasma actuation frequency should be adjusted to increase the local velocity gradient, ensuring consistent fluid deformation and preventing sudden changes or reverse flow. The proposed control strategies work synergistically to address vortex asymmetry from multiple perspectives. Vortex interaction regulation targets global dynamics, reducing induced velocity to balance the vortex spatial structure. In contrast, flow field stability optimization and velocity gradient control improve local stability by maintaining appropriate Jacobian and divergence, suppressing disturbance growth, and preserving flow field symmetry. These asymmetric vortex control strategies provide a framework for designing plasma actuators in the next section.

III. Results and discussion

A. Experimental setup and plasma actuator design

The intelligent closed-loop control algorithm was trained online using the educational open-return wind tunnel at Xi'an University of Technology, China. The wind tunnel is 1.545 m long and 0.5 m wide, with a rectangular test section measuring 0.35 m × 0.22 m (see **Figure 2**). The wind tunnel speed is adjustable between $U_{\infty} = 5 \sim 15$ m/s, with a turbulence level of $\varepsilon \leq 2\%$. The slender body model consists of a detachable conical forebody and afterbody, forming a circular cone for testing. The model was 3D-printed with Polylactic Acid (PLA) for its excellent electrical insulation and thermal deformation resistance required for plasma discharge. The model has a total length of L = 150 mm, a base diameter of $D = 55$ mm, and a 10° semi-apex angle. The 3D printing precision was less than 0.1 mm to ensure geometric accuracy. During the experiments, the angle of attack was set to $\alpha = 45°$, with the sideslip angle fixed at zero. At a freestream velocity of 10 m/s, the Reynolds number based on the model's base diameter was approximately 3.76×10^4.

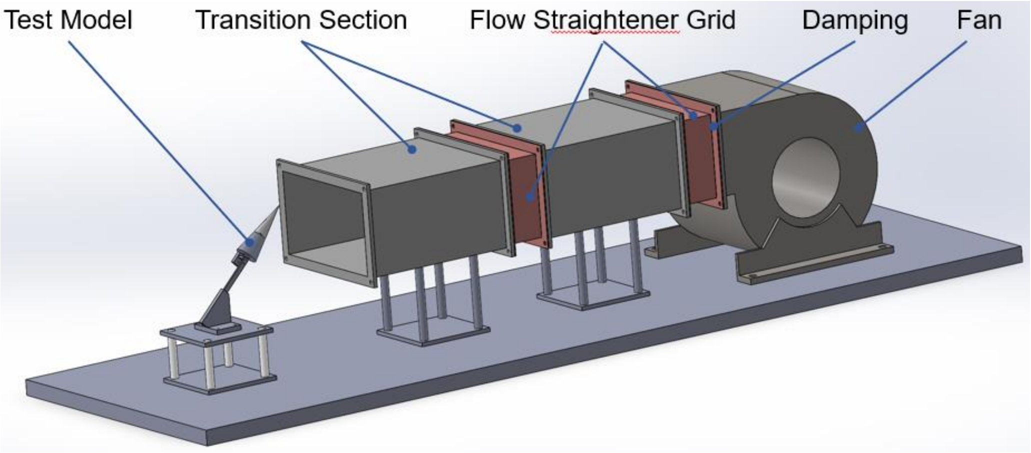

Figure 2　Schematic diagram of the educational open-return wind tunnel

Based on the system stability conditions in “II. Control Strategy Analysis”, the design methods for the DBD plasma actuator are analyzed from three perspectives: structural optimization, interference mitigation, and control optimization. Corresponding strategies are proposed to address the specific issues:

(1) Symmetric Structure (Symmetric Position Design): Plasma discharge induces vortices along the slender body surface, injecting transverse velocity into the boundary layers and triggering boundary layer transition **22**. This artificial induced symmetric vortex suppresses the natural asymmetric vortices, reducing the randomness of lateral forces. Symmetric vortices generate a near-zero transverse velocity gradient $\partial v/\partial y$, balancing the velocity distribution and minimizing vortex-induced lateral force asymmetry. This prevents the divergence D_0 from increasing, thus ensuring flow stability by suppressing local disturbances. Furthermore, the symmetric layout maintains $\partial v/\partial y > 0$, ensuring symmetry in other velocity gradient components, and optimizing the Jacobian $J_0 > 0$ to stabilize the vortex system. **(2) Interference Mitigation** (**Maximum Distance Design**): According to the vortex interaction principle described in Equation (1), this design can reduce interference between vortex pairs, which can be achieved by decreasing vortex circulation (Γ) to weaken induced velocity or increasing vortex spacing (r) to minimize local flow disturbances. Reducing vortex circulation and weakening induced velocity appropriately mitigate local flow disturbances, ensuring the condition $J_0 > 0$ is satisfied. **(3) Control Optimization**

(counterflow blowing design): Counterflow blowing effectively controls asymmetric vortices under certain conditions, but excessive plasma injection energy reduces control efficiency [29-30]. Excessive crossflow blowing increases the longitudinal velocity gradient $\partial u/\partial x$, leading to $D_0 > 0$ and system instability. Combining crossflow blowing with optimized transverse blowing reduces $\partial v/\partial y$, balancing the increased divergence D_0. Suppressing secondary velocity gradient components mitigates adverse effects on the Jacobian J_0, thereby improving control effectiveness and system stability.

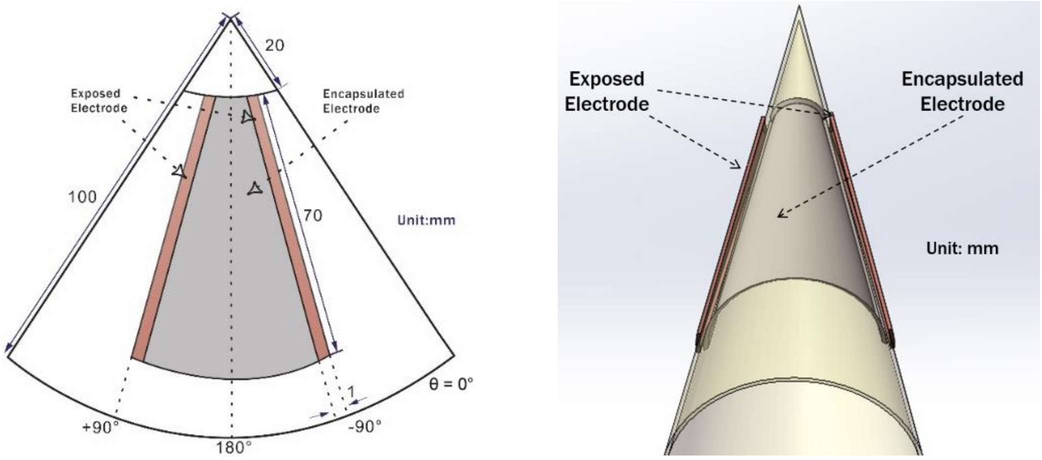

(a) 2D schematic of electrode arrangement (b) 3D model of actuator placement

Figure 3 Three-electrode DBD actuator for asymmetric vortex control on a slender body

This study developed a novel three-electrode dielectric barrier discharge (DBD) plasma actuator following the above principles. All electrodes were made from 0.03 mm thick copper foil and manually cut into the specified configuration. The insulating layer comprised three layers of polyimide film (Kapton), each 0.07 mm thick, theoretically withstanding up to 50 kV and providing sufficient insulation under a 16 kV pulsed plasma discharge. Additionally, Kapton was selected for its high thermal resistance, chemical stability, and mechanical flexibility, making it ideal for plasma actuator applications. Two strip-exposed electrodes, each 70 mm long and 1 mm wide, were symmetrically positioned at circumferential angles of $\theta = \pm 90°$ along the slender body's 180° centerline. This design maximizes the discharge distance and generates symmetrical induced vortices. The two exposed electrodes share a fan-shaped encapsulated electrode beneath the insulating layer (gray area in Figure 3), allowing the plasma actuators on both sides of the slender body to induce vortices toward the leeward centerline.

Early experiments with plasma actuators installed near the conical nose revealed several issues: arc discharge from reduced electrode spacing leading to equipment degradation, passive flow control effects from geometric modifications interfering with active flow control, and installation complexity on curved surfaces affecting discharge stability. While placing actuators closer to the apex enhances control, excessive proximity increases the risk of arc discharge. After extensive testing, the plasma actuator was optimally positioned 20 mm from the cone apex, balancing control effectiveness and safety while reducing equipment degradation risks.

This new three-electrode DBD plasma actuator introduces symmetric plasma disturbances before the natural separation points on the slender forebody. These disturbances induce symmetric boundary layer separation on both sides, forming symmetric vortices and suppressing naturally generated asymmetric vortices. In contrast, the control strategy in Ref. [18] injects unequal plasma energy on both sides of the slender forebody, modulating the strength of naturally generated asymmetric vortices. This approach focuses on balancing asymmetric forces rather than preventing them. Compared to Ref. [18], this study's symmetric plasma disturbances enhance stability by ensuring symmetric boundary layer separation before the natural separation points, thereby preventing the formation of asymmetric vortices.

B. Closed-loop Plasma Control System for Lateral Force Regulation

Figure 4 shows the signal flow of the closed-loop plasma control system. The primary function of the system is to use real-time lateral force signals of the slender body to control asymmetric vortices via plasma actuation, enabling precise lateral force regulation. The system consists of three main components: the data acquisition module, the control module, and the data processing module.

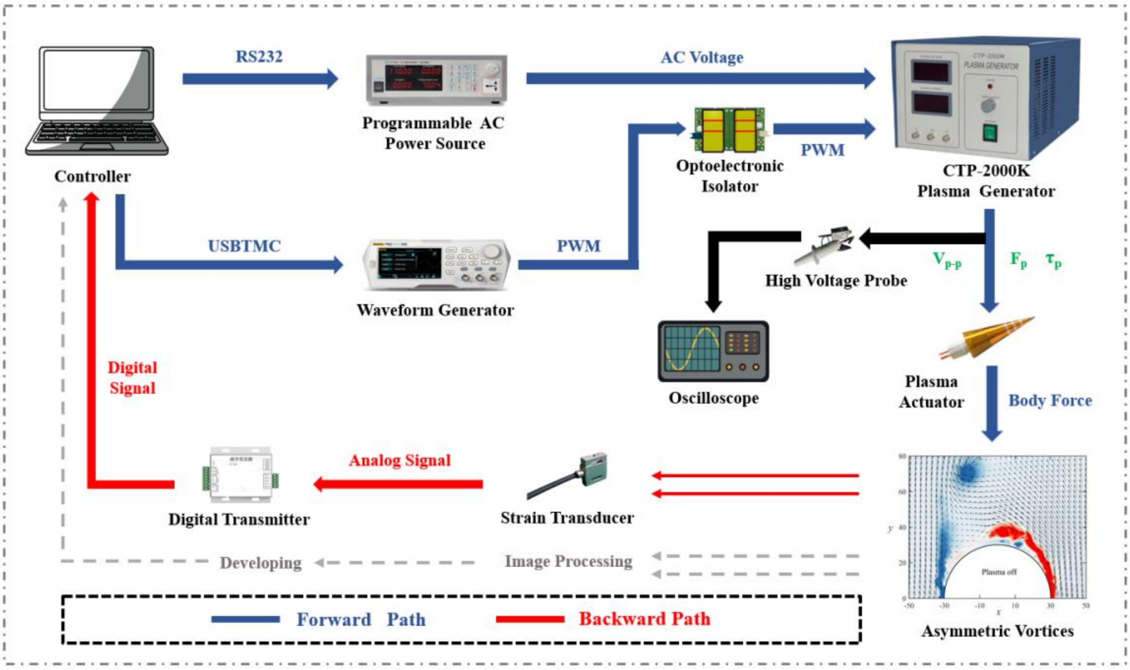

Figure 4 Closed-loop control system with signal flow for forebody asymmetric vortices

(1) Data Acquisition Module: A strain transducer (AUTODA Co., AT8301, 1N range, 3.1 kHz sampling frequency, 2×10^{-5} N precision) measures the lateral force on the slender body and transmits it as an analog signal to the digital transmitter. The digital transmitter converts the analog signal into a digital signal, which is sent to the controller. The strain transducer was installed inside the rear section of the slender-body model and directly connected to a 3D-printed PLA support rod, allowing for direct measurement of the lateral force acting on the slender body. **(2) Control Module**: The controller, equipped with an Intel Core i7-12700KF processor, 64GB DDR4 memory, and an Nvidia 4060 Ti GPU, serves as the host hardware platform. The development environment includes Python 3.9 and PPO-compatible libraries, with PyCharm and NI LabVIEW as integrated development environments (IDEs). The controller processes lateral force data and generates control commands, which are sent to the programmable AC power source via RS232 and the waveform generator via USBTMC. **(3) Data Processing Module**: The waveform generator produces pulse-width modulation (PWM) signals to define plasma parameters such as actuation voltage, duty ratio, and pulse frequency. These PWM signals are transmitted to the CTP-2000K plasma generator, which amplifies the PWM signals into high-voltage AC signals. An optoelectronic isolator ensures safe signal transmission between the waveform generator and the CTP-2000K plasma generator, preventing high-voltage reverse breakdown and protecting the closed-loop control system. The high-voltage AC signals are monitored by a high-voltage probe and a digital oscilloscope. These high-voltage signals drive the DBD actuators, generating plasma discharge to inject energy into the flow field.

The DBD plasma actuator regulates the spatial structure of asymmetric vortices over the slender body in real-time to reduce asymmetry and adjust the lateral force. The updated lateral force is measured by the strain transducer and fed back to the controller for further processing. The closed-loop control system continuously adjusts actuation parameters until the lateral force reaches the desired value. In the educational open-return wind tunnel experiments, PPO successfully achieved real-time closed-loop control, with each inference-based policy update requiring approximately 6.32 s. From detecting lateral force variations to plasma actuation, the total response time was approximately 3 seconds, including sensor data acquisition, PPO inference, signal transmission, and plasma discharge delay. The forward path (in blue) generates and delivers plasma actuation signals, driving the DBD plasma actuator to modulate asymmetric vortices. The feedback path (in red) processes real-time data acquisition and dynamically adjusts control parameters, ensuring efficient and precise closed-loop performance.

Deep reinforcement learning (DRL) has demonstrated significant potential in controlling complex fluid dynamics due to its capability to optimize control strategies for nonlinear, high-dimensional, and time-varying systems [31-32]. Standard deep reinforcement learning algorithms include DQN[33-34] (Deep Q-Network), DDPG[35] (Deep Deterministic Policy Gradient), TRPO[36-37] (Trust Region Policy Optimization), and PPO (Proximal Policy Optimization). DQN, based on Q-learning, employs a deep neural network to approximate the Q-value function. It is effective for discrete action spaces but suffers from unstable updates and is not suitable for continuous action spaces. DDPG extends DRL to continuous action spaces but is highly sensitive to noise, susceptible to local optima, and often results in unstable training. TRPO improves training stability by constraining policy updates, but its optimization process is computationally expensive and complex. In contrast, PPO simplifies TRPO's optimization process by introducing clipping technology while retaining its stability benefits. PPO's capacity for stable policy updates and efficient exploration in nonlinear, high-dimensional, and time-varying environments, make it a promising candidate for asymmetric vortex control. These characteristics enable PPO to handle the complexity and uncertainty inherent in vortex dynamics by ensuring training stability, limiting policy update steps, and adapting to dynamic flow field changes. Therefore, this paper adopts the PPO algorithm to optimizing plasma actuation parameters for asymmetric vortex control.

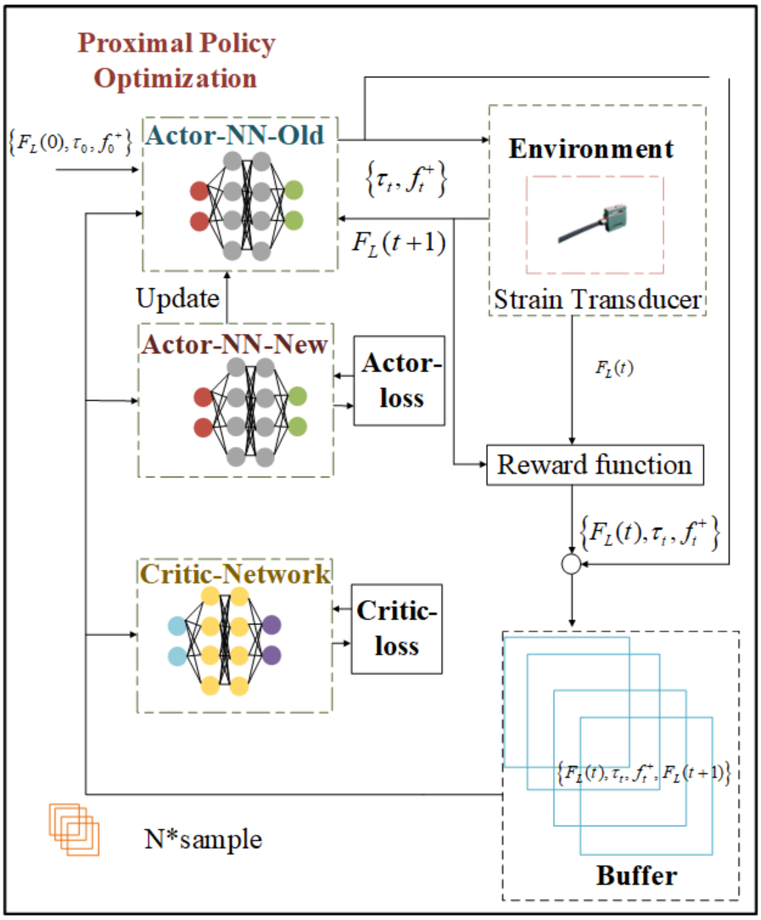

Figure 5 PPO-based closed-loop control framework for lateral force regulation

The PPO online training process consists of three steps: data acquisition, data processing, and control parameter optimization. The lateral force signal is initially collected in real-time by a strain transducer and processed in LabVIEW with a digital low-pass filter to reduce noise and ensure data quality. LabVIEW processes the lateral force signal and preset actuation parameters, then transmits the processed data to the self-developed PPO Python program for further analysis and control. The PPO algorithm generates updated plasma control parameters, including duty cycle and pulse frequency, which are dynamically adjusted in real-time to regulate the lateral force.

Figure 5 illustrates the signal flow between key modules, including signal acquisition (lateral force measurement), parameter generation and updating (duty cycle and pulse frequency), and control parameter optimization. The PPO algorithm comprises two components: the Actor and the Critic network. The environment state includes real-time lateral force signals and current control parameters. The Actor network (comprising Actor-NN-Old and Actor-NN-New) generates updated control parameters based on these states, optimized by minimizing the Actor-Loss. The Critic network evaluates the effectiveness of the current state and control parameters using a reward function and enhances training stability by minimizing the Critic-Loss. The reward function aims to minimize the lateral force signal by optimizing the duty cycle and pulse frequency, incorporating weighting coefficients to balance the priorities of multiple optimization objectives. The Buffer module stores training samples to improve sample efficiency through experience replay, thereby enhancing training stability and accelerating convergence. By incorporating real-time feedback into the reward evaluation process and iteratively optimizing policy updates, the PPO algorithm achieves closed-loop control of the flow field around the slender body in nonlinear, time-varying environments.

The input parameters for the PPO algorithm includes the time-varying lateral force and the predefined adjustment ranges for the duty ratio and reduced frequency, which are utilized to optimize plasma actuation parameters.

State Space:

$$S_t = \left\{ F_L(t), \tau_t, f_t^{+} \right\} \tag{5}$$

Here, $F_L(t)$ represents the time-varying lateral force signal collected by the strain transducer, $\tau_t = \left\{ \tau_{t-n}, \tau_{t-n-1}, \cdots, \tau_t, \tau_{t+1}, \tau_{t+2}, \cdots, \tau_{t+n} \right\}$ represents the duty ratio of the modulation signal, which defines the proportion of plasma discharge time to the total duration of a modulation cycle. $f^+ = \left\{ f_{t-n}^+, f_{t-n-1}^+, \cdots, f_t^+, f_{t+1}^+, f_{t+2}^+, \cdots, f_{t+n}^+ \right\}$ represents the reduced frequency ($f^+ = 2\pi f_p d / U_\infty$, where f_p is the pulse frequency and d = 59.95 mm is the local diameter of the slender body at the first pressure measurement station).

Action Space:

$$a_t = \left\{ \tau_t, f_t^+ \right\} \tag{6}$$

Among them, $\tau_t \in (1\%, 100\%)$ denotes for the duty ratio of the plasma actuation modulation signal, $f_t^+ \in (0.377, 376.8)$ characterizes the action space defined by the range of reduced frequency.

A dual-network structure based on the Actor-Critic framework to optimize plasma actuation parameters had been employed. The Actor network outputs a probability distribution over the action space to guide the selection of optimal actuation parameters, while the Critic network evaluates the system's current state and outputs a scalar value to refine policy updates. Both networks consist of three fully connected layers with 256, 128, and 64 neurons, respectively. ReLU activation is applied to all hidden layers, and no activation function is used in the output layers to allow continuous outputs suitable for plasma control. Table 1 is the specific related hyperparameters.

Table1 Proximal Policy Optimization (PPO) training hyperparameters.

Hyperparameter	Setting
Learning Rate	3e-4
Gamma	0.95
Lambda	0.95
Clip Range	0.2
Epoch	4
Horizon	2048

The reward function is designed to minimize the lateral force signal, a key indicator of control performance. Additionally, a weighting factor α is incorporated to balance lateral force reduction and energy efficiency, ensuring the PPO algorithm optimizes both control effectiveness and power consumption (Equation 7). The real-time lateral force signal directly influences the reward function, guiding the policy refinement process. Here, F_L denotes the real-time scalar lateral force signal.

$$R_1 = -\alpha F_L \tag{7}$$

The final total reward function is the control target reward:

$$R = R_1 \tag{8}$$

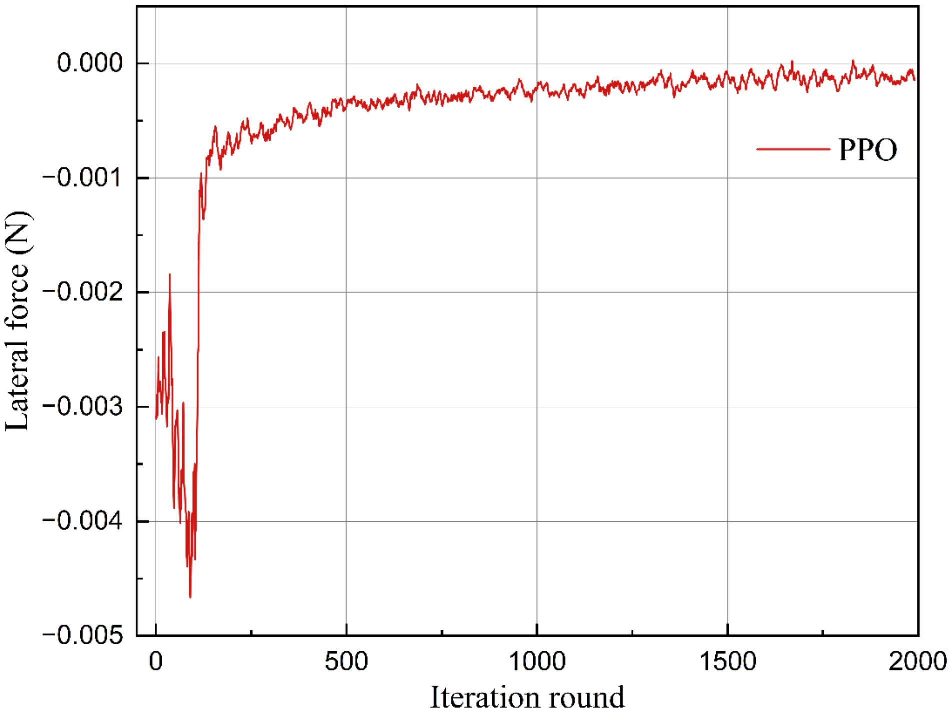

Figure 6 PPO convergence curve of for lateral force control

Figure 6 illustrates the lateral force convergence curve of the PPO algorithm's training. The initial setup for online training included baseline actuation parameters for duty ratio and pulse frequency, along with initial lateral force measurements. During training, a learning rate of 0.0003 and a batch size of 64 were used, with each training iteration taking approximately 5 minutes. The curve converges after approximately 1800 training iterations, demonstrating the control system's ability to enhance flow field symmetry and performance. This result highlights the closed-loop control system's capability to significantly improve flow field symmetry, as reflected by the optimized plasma actuation parameters and reduced lateral force.

C. Wind tunnel experiments with synchronized pressure and PIV measurements

Validation experiments were conducted in a low-speed closed-return wind tunnel to verify the optimal plasma actuation parameters obtained through online training in the educational open-return wind tunnel. The spatiotemporal evolution of plasma-induced vortices and asymmetric vortex interactions was analyzed through synchronized pressure and particle image velocimetry (PIV) measurements. The wind tunnel and testing equipment in this paper are similar to those described in Refs. **23-24**, but with refinements in the experimental model and methods to enhance data accuracy. While multi-electrode plasma actuators were previously employed in open-loop control systems, their reliance on multiple high-voltage power supplies complicated system design and operation, limiting practical engineering applications. To facilitate research on intelligent closed-loop control systems, this study simplified the plasma actuator design by adopting a single AC power supply and focused on evaluating the control effects of plasma actuation on the physical parameters of forebody asymmetric vortices.

Experiments were performed in a low-speed closed-return wind tunnel, measuring 19.79 m in length and 10.16 m in width. The test section was 3 m long with a cross-section of 1.2 m × 1.0 m (Figure 7(a)). The wind tunnel speed was adjustable from $U_\infty = 5 \sim 75$ m/s with a turbulence level of $\varepsilon \leq 0.2\%$. Three interchangeable glass windows in the test section facilitated PIV optical diagnostics. The slender body model consisted of a circular cone and a cylindrical afterbody (Figure 7(b)), constructed from Bakelite for its thermal resistance and mechanical stability, with a total length of $L = 500$ mm. The circular cone had a 10° semi-apex angle, and the cylindrical afterbody had a base diameter of $D = 120$ mm. The angle of attack was set to $\alpha = 45°$, with a sideslip angle fixed at zero. The free-stream velocity U_∞ was set to 10 m/s, corresponding to a Reynolds number of 0.81×10^5 based on the model's base diameter.

(a) (b)

Figure 7 The experimental setup in the low-speed closed-return wind tunnel. (a) Wind tunnel, data acquisition, and slender body model layout; (b) Front and side views of the slender body model

Surface pressure measurements conducted to assess flow control performance. Four pressure measurement stations were placed along the model at 20 mm intervals. Each station was equipped with 24 pressure transducers, circumferentially distributed at azimuth angle intervals of $\Delta\theta = 15^\circ$. The experiments utilized Model 9816 pressure transducers (PSI Company), operating at a 100 Hz sampling frequency with an accuracy of below 0.1%. For each condition, continuous 10-second recordings from steady pressure transducers were collected for data analysis. Three repeated measurements verified the consistency of pressure distributions, with fluctuations primarily attributed to equipment noise rather than flow instability. Standard deviation analysis showed pressure coefficient variations within ±0.02, consistent with sensor accuracy, ensuring the reliability of the data. The right side of the cone, facing the free stream, was defined as the starboard side, while the left side was designated as the port side. The windward side corresponded to an azimuth angle of $\theta = 0^\circ$, with counterclockwise rotation defined as positive.

A two-dimensional PIV system was utilized to visualize the detailed vortex structure of the flow field around the slender body. Flow images were captured using a 2048×2048 pixel^2 CCD camera with a 100×80 mm^2 field of view, at an acquisition frequency of 5 Hz. The recorded data were processed using Insight 3G software. The final interrogation window size was set to 32×32 pixels^2 with a 75% overlap ratio to ensure high spatial resolution. The entire wind tunnel test section was seeded with smoke particles of 1 μm mean diameter for flow visualization. PIV measurements were conducted at the 1.25D cross-section ($L = 150$ mm), corresponding to the first pressure measurement station. To enhance PIV measurement accuracy, several optimizations were applied. The measurement region was centered to minimize perspective errors, and the slender body model was coated with black matte paint to reduce laser reflection, enhancing near-wall velocity measurements. Appropriate tracer particles were selected to minimize lag effects, and the time interval was optimized for precise velocity calculations. PIV data were continuously recorded for 10 seconds per case with a 200 μs delay, beginning after 300 seconds of flow stabilization to ensure reliability.

A high-voltage sinusoidal AC wave source (CTP-2000K, CORONA Lab.) was used to generate DBD plasma actuation, with a peak-to-peak voltage of $V_{AC} = 16$ kV. The carrier frequency was set between $F = 7.5$ kHz. The encapsulated electrode was grounded. The pulsed frequency (f_p) was varied from 1 Hz to 1,000 Hz to investigate the dynamic interactions between plasma-induced vortices and forebody asymmetric vortices. The duty ratio (τ) was varied from 1% to 100% to study its effects on pressure distribution and lateral force.

Table 2 Actuation modes and reduced frequencies in six test cases.

Case	Actuation Mode	Reduced Frequency
1	Plasma off (baseline)	/
2	Steady actuation	/
3	OL - f_{p1} optimization	0.75
4	OL - f_{p2} optimization	7.5
5	OL - f_{p3} optimization	75
6	Closed-loop optimization	22.62

The vortex shedding frequency behind a slender body at high angles of attack refers to the periodic detachment or movement of asymmetric primary or secondary vortices along the leeward side. While similar to the Kármán vortex street observed behind cylindrical bodies, the vortex shedding in slender bodies is more irregular and unstable due to their geometry and the complexity of high-angle-of-attack flows. This frequency is typically represented by the Strouhal number (*St*), defined as $St = fD / U_\infty$, where f is the shedding frequency (Hz), D is the characteristic length (e.g., base diameter), and U_∞ is the freestream velocity. For slender bodies, *St* number usually ranges from 0.1 to 0.2 depending on factors such as angle of attack, Reynolds number, and the geometric shape and dimensions of the slender body model. Based on experimental parameters ($d = 59.95$ mm (diameter of the first pressure station of the slender body); $U_\infty = 10$ m/s (freestream velocity); Angle of Attack = 45°), the estimated vortex shedding frequency ranges from 16.68 to 33.36 Hz, corresponding to a reduced frequency of $f^+ = 0.628 - 1.256$.

Six representative cases were selected for flow field analysis to systematically evaluate the plasma control effectiveness on forebody asymmetric vortices (Table 2). Case 1 represents the baseline condition without plasma actuation. Case 2 corresponds to steady plasma actuation, a commonly used early method. Later studies showed that pulsed plasma actuation offers better control performance with higher energy efficiency [29-30]. Cases 3-5 are based on Case 2, with open-loop (OL) control optimized for duty ratio and pulse frequency to modulate plasma energy input. The duty ratio controls the energy intensity of the plasma-induced jet, determining the energy injected into the flow field. Meanwhile, an appropriate pulse frequency can couple plasma actuation with the natural vortex shedding frequency, potentially creating a resonance-like effect. This coupling effect enhances flow control effectiveness by amplifying vortex interactions with minimal energy input. In Case 6, optimized actuation parameters obtained from closed-loop online training in the educational open-return wind tunnel are validated in the low-speed closed-return wind tunnel to assess their adaptability and effectiveness. The selection of reduced frequency f^+ in Cases 3-5 investigates plasma actuation effects across various frequency ranges. Case 3 ($f^+ = 0.75$) aligns with the natural vortex shedding frequency, potentially inducing resonance effect. Case 4 ($f^+ = 7.5$) enhances plasma-vortex interaction, whereas Case 5 ($f^+ = 75$) disrupts vortex coherence. Experiments were conducted under identical conditions, with synchronized PIV and pressure measurements ensuring accuracy. Case 6 ($f^+ = 22.62$), employing closed-loop optimization, further validates the effectiveness of adaptive plasma control.

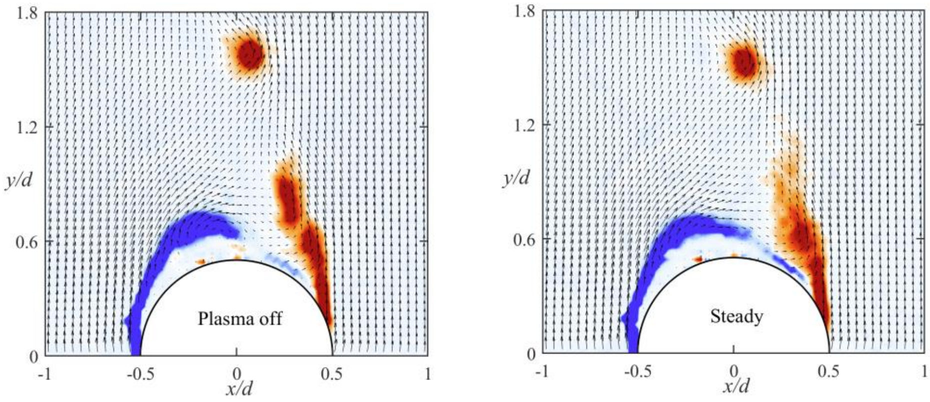

(a) Case 1 (b) Case 2

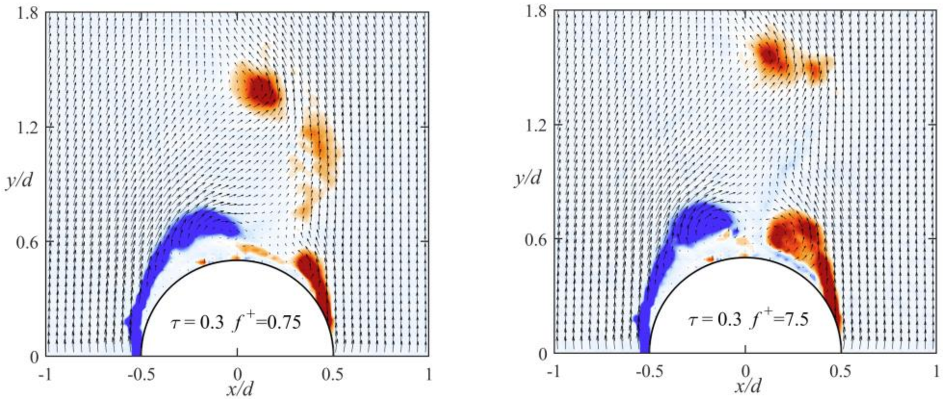

(c) Case 3 (d) Case 4

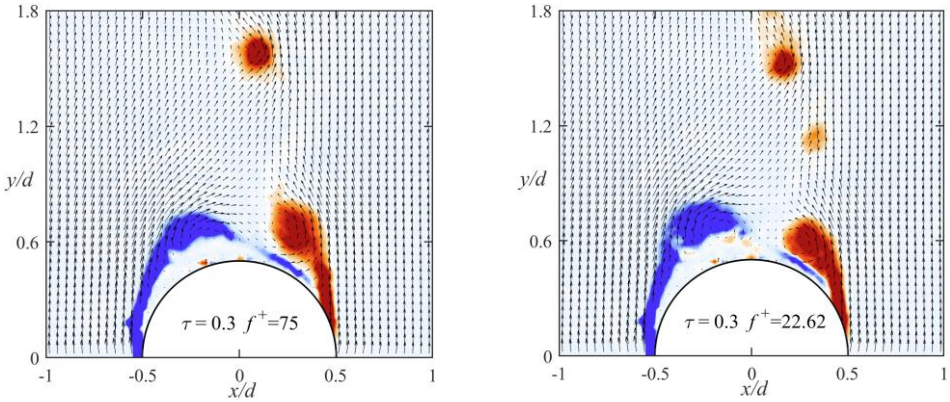

(e) Case 5 (f) Case 6

Figure 8 PIV Time-averaged axial-vorticity contours for different actuation cases

Figure 8 illustrates the PIV flow field at the first pressure measurement station ($x/L = 0.283$), showing the spatial distribution of the asymmetric vortex structure. When the plasma actuators are inactive (Case 1), the left vortex (blue) is positioned near the model surface with negative vorticity and counterclockwise rotation), while the right vortex (red) is farther from the model surface with positive vorticity and clockwise rotation, creating an asymmetric spatial pattern (Fig. 9(a)). Additionally, at a location far from the wall ($x/d = 0.08$, $y/d = 1.58$), a detached vortex evolves from the primary vortex on the right side, subsequently stabilizing as part of the flow field around the slender body. Since the detached vortex is located beyond twice the local sectional radius from the slender body surface, its influence on the lateral force is negligible [5]. Therefore, the following discussion will focus on the effects of near-wall primary vortices on both sides of the slender body and their influence on lateral force and stability.

In Case 2 (Fig. 8(b)), with steady plasma actuation, the vortex strength on both sides diminishes, and the right-side vortex diffuses significantly. This indicates that steady mode reduces lateral force by weakening the vorticity on both sides of the slender body, although the overall symmetry is not fully restored. In open-loop (OL) mode (Cases 3-5, Figs. 8(c-e)), the reduced frequency f^+ ($f^+ = 2\pi f_p d / U_\infty$,where f_P is the pulse frequency and $d = 59.95$ mm is the diameter of the first pressure station of the slender body) is varied to examine its effect on vortex dynamics. In flow control, the reduced frequency is often used to characterize flow fields influenced by plasma actuation, while the Strouhal number is generally used to describe natural vortex shedding frequencies.

As f^+ increases from 0.75 (Case 3, Fig. 8(c)) to 7.5(Case 4, Fig. 8(d)), the strength of the counterclockwise blue vortex on the left side gradually increases from $\omega_z = -3154.99 s^{-1}$ to $\omega_z = -2891.48 s^{-1}$. However, when f^+ increases to 75 (Case 5, Fig. 8(e)), the vorticity of the blue vortex on the left $\omega_z = -2891.48 s^{-1}$ decrease to $\omega_z = -3119.16 s^{-1}$ with coordinates at $x/d = -0.25$, $y/d = 0.66$. This demonstrates that completely eliminating lateral force through open-loop control requires iterative parameter adjustments to approach the desired results. However, changes in experimental conditions can alter the natural flow field, rendering previously obtained open-loop control parameters ineffective and necessitating a new optimization process.

In Case 6 ($f^{+} = 22.62$), the optimal actuation parameters from online closed-loop training are applied to the low-speed closed-return wind tunnel. Despite differences in temperature, humidity, model dimensions, and Reynolds number between the two wind tunnel experiments, the geometric similarity of the slender body model and the spatiotemporal evolution of asymmetric vortices provide the foundation for actuation parameter transferability. The PIV results in Fig. 8(f) confirm that the vortices on both sides of the slender body exhibit near symmetry in spatial structure and strength, demonstrating the effectiveness of the closed-loop control system. However, further analysis is required to evaluate the pressure distribution, lateral force reduction, and vortex stability to validate the control performance. Although the results highlight the potential for actuation parameter transferability, nonlinear effects caused by experimental condition differences may still affect control accuracy.

Figure 9 shows the time-averaged surface pressure distribution at the first pressure measurement station ($x / L = 0.283$). When the plasma actuators are inactivated (Case 1), the suction peak on the port side ($C_p = -1.31$ at $\theta = 165°$) is higher than that on the starboard side ($C_p = -0.35$ at $\theta = 300°$), indicating stronger and closer vortices on the left side. This asymmetric distribution is consistent with the PIV results in Fig. 8(a). Under steady plasma actuation (Case 2), the suction peak on the port side decreases slightly, suggesting limited control effectiveness in reducing lateral force. In open-loop control (Cases 3-5), the pressure distribution evolves toward a mirror-imaged asymmetric bistable pattern. Notably, a higher reduced frequency does not always lead to greater changes in pressure distribution or stronger control effectiveness over the asymmetric vortices. Case 5 ($f^{+} = 75$) demonstrates a weaker control effect on pressure distribution compared to Case 4 ($f^{+} = 7.5$), but still stronger than steady actuation (Case

3). This confirms that there exist optimal pulse frequencies which can maximizes the plasma actuation's effectiveness in controlling the asymmetric vortices [30].

Case 6 ($f^{+}=22.62$) demonstrates the most effective control, achieving a near-symmetric pressure distribution using optimal actuation parameters from online closed-loop training. The mechanism of plasma actuation lies in injecting energy tangentially into the boundary layer, altering transition points and restructuring the spatial organization of asymmetric vortices. Compared to the open-loop control cases (Cases 3-5), Case 6 exhibits the most effective control over the asymmetric vortices. However, transferring actuation parameters from the open-return wind tunnel to the closed-return wind tunnel introduced minor deviations, preventing complete lateral force elimination. Future studies should develop adaptive algorithms to dynamically adjust actuation parameters and expand the applicability of the closed-loop control strategy to various wind tunnels.

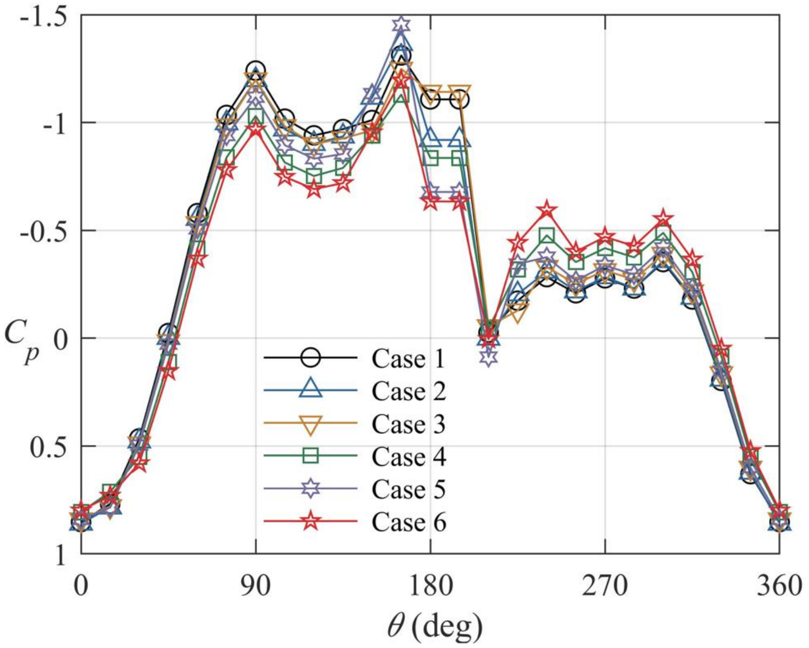

Figure 9 Time-averaged surface pressure distribution under different actuation cases

Table 3 provides a detailed comparison of the local and overall lateral force coefficients for the slender model under various plasma actuation modes. In Case 1 (plasma off), the flow field exhibits a pronounced asymmetric vortex structure, resulting in a baseline local lateral force coefficient ($C_{yd1}=0.533$) at the first pressure measurement station ($x/L = 0.283$). The variation rate in local (ΔC_{yd}) and total (ΔC_y) lateral force coefficient is quantified relative to Case 1, as calculated by Equations (9) and (10). C_{ydn} and C_{yn} represents the local and total lateral force coefficient for Cases 2-6, where n ranges from 2 to 6.

$$\Delta C_{yd} = \frac{C_{ydn} - C_{yd1}}{C_{yd1}} \tag{9}$$

$$\Delta C_y = \frac{C_{yn} - C_{y1}}{C_{y1}} \tag{10}$$

Table 3 Lateral force coefficients and reduction rates under different cases

Case	1	2	3	4	5	6
C_{yd}	0.533	0.509	0.462	0.255	0.421	0.160
$-\Delta C_{yd}$	0	4.50%	13.9%	60.2%	43.9%	88.6%
$-\Delta C_y$	0	15.7%	27.6%	64.5%	35.5%	84.2%

Table 3 shows that under steady plasma actuation (Case 2), the local lateral force coefficient decreases slightly ($\Delta C_{yd} = -4.50\%$), indicating limited control effectiveness, as the asymmetric vortex structure remains largely unchanged. This result aligns with the pressure distribution and PIV measurements in Fig. 9(a) and Fig.10. As the reduced frequency (f^+) increases under open-loop control (Case 3-5), the lateral force coefficient does not vary linearly but achieves best suppression in Case 4 ($f^+ = 7.5$) with $\Delta C_{yd} = -60.2\%$, and $\Delta C_y = -64.5\%$. However, closed-loop control (Case 6, $f^+ = 22.62$) demonstrates superior performance, achieving reductions of $\Delta C_{yd} = -88.6\%$ and $\Delta C_y = -84.2\%$. Compared to steady plasma actuation (Case 2), the PPO-based algorithm in Case 6 achieves a 68.5% reduction in total lateral force coefficient, while energy consumption decreases by 70% (Case 2, $\tau = 100\%$; Case6, $\tau = 30\%$). These findings highlight the closed-loop control as an effective and energy-efficient solution for asymmetric vortex control, demonstrating its potential for aerodynamic stability enhancement in engineering applications.

Based on the theory in Section II. "Control strategy analysis", the vortex stability depends on their local dynamic characteristics, with the Jacobian and divergence serving as key physical parameters. Stationary point with $D_0 < 0$ and $J_0 > 0$ exhibit decaying flow disturbances, reducing asymmetric vortex formation. Table 4 summarizes the stability analysis of stationary points (x_0, y_0) across six plasma actuation modes, which are determined by solving the conditions $u(x, y) = 0$ and $v(x, y) = 0$, where u and v are the velocity components in the respective directions. These stationary points correspond to critical regions in the vortex structure where the local velocity vanishes, making them highly sensitive to flow stability changes. Point 1 is located on the port (left) side, representing the stronger vortex core closer to the wall, while Point 2 is on the starboard (right) side, corresponding to the weaker vortex core slightly farther from the wall. The selection of these points facilitates a detailed evaluation of plasma actuation's effect on vortex asymmetry and stability.

In Case 1 (plasma off), both the Jacobian and divergence at Point 1 are negative ($J_0 = -0.09$, $D_0 = -0.66$), indicating a typical unstable state, susceptible to external minor disturbances and leading to vortex instability. In contrast, Point 2 shows weak stable ($J_0 = 0.05$, $D_0 = -0.09$), though it remains vulnerable to external perturbations due to low absolute values.

In Case 2 (steady plasma actuation), steady actuation continuously inject energy along both sides of the slender body in the upstream direction, aiming to reduce asymmetry in the vorticity gradients. For Point 1, the Jacobian approaches zero ($J_0 = 0.01$, $D_0 = 0$), indicating a state of neutral stability with oscillatory behavior under steady actuation. However, the divergence of Point 2 decreases further ($D_0 = -0.1$), slightly enhancing stability. Steady plasma actuation has limited effectiveness in improving flow symmetry.

In Cases 3-5 (OL pulsed plasma actuation), the flow dynamics are significantly altered as the reduced frequency (f^+) increases. At $f^+ = 7.5$ (Case 4), the control effect reaches its peak, with maximum values of $J_0 = 1.10$, $D_0 = 0.25$, indicating significant enhancements in local vortex stability. However, further increases in reduced frequency to $f^+ = 75$ (Case 5), disrupt the energy balance in the flow field, leading to diminished control effectiveness. This suggests that excessive actuation frequency may exceed the controllable range of the asymmetric vortices' dynamic characteristics. Optimizing the pulsed frequency further could help improve the vortex system's stability.

Table 4 Stability analysis of stationary points under different cases

Case	**Coordinate** ($x_0/d, y_0/d$)	**Jacobian** (J_0)	**Divergence** (D_0)	**Stability**
1	P1(−0.085,0.641)	-0.09	-0.66	Unstable
	P2(0.213,0.875)	0.05	-0.09	Stable
2	P1(−0.085,0.617)	0.01	0.00	Neutral stability (oscillation)
	P2(0.257,0.705)	0.04	-0.10	Stable
3	P1(−0.107,0.640)	0.16	0.01	Unstable
	P2(0.321,0.470)	0.37	-0.22	Stable
4	P1(−0.1708,0.6407)	0.51	0.14	Unstable
	P2(0.1708,0.5765)	1.10	0.25	Unstable
5	P1(−0.085,0.641)	-0.15	-1.13	Unstable
	P2(0.235,0.661)	0.37	-0.09	Stable
6	P1(−0.170,0.663)	0.89	0.13	Unstable
	P2(0.257,0.597)	0.86	-0.12	Stable

In Case 6 (closed-loop control), dynamic optimization of actuation parameters is achieved using the PPO algorithm. Although the Jacobian and divergence ($J_0 = 0.86$,

$D_0 = -0.12$) are slightly lower than those in Case 4 (open-loop control), the vortex system exhibits improved stability and enhanced energy dissipation. Compared to steady plasma actuation (Case 2), closed-loop control significantly increases the Jacobian and reduces the divergence, effectively optimizing the flow gradient. This leads to an 68.5% reduction in total lateral force coefficient and a 70% reduction in energy consumption. These results highlight the high practical value of closed-loop control for engineering applications, particularly for achieving stable and energy-saving vortex regulation in flight control systems.

In this study, the closed-loop control system optimized the plasma actuation reduced frequency $f^+ = 22.62$, corresponding to an actual pulse frequency of 300 Hz. Compared to the natural vortex shedding frequency (16.68-33.36 Hz), the plasma actuation frequency is approximately ten times higher. Despite this significant discrepancy, experimental results demonstrate that plasma actuation effectively controls the formation and evolution of asymmetric vortices. This suggests that complex coupling mechanisms exist between the high-frequency actuation and the vortex system. Preliminary explanations are as follows:

High-frequency plasma actuation may effectively control the formation and evolution of asymmetric vortices through various mechanisms. First, high-frequency actuation may resonate with secondary instability modes within the vortex system, indirectly enhancing the stability of the primary vortices. Second, even if the actuation frequency does not match the natural vortex shedding frequency, high-frequency plasma actuation can disrupt the coherence required for vortex formation, suppressing asymmetric vortices' development. Additionally, high-frequency actuation may induce nonlinear interactions with low-frequency vortex shedding, such as modulating the strength and phase of low-frequency vortices or triggering subharmonic responses, indirectly influencing vortex-shedding behavior. Finally, the optimization results of the closed-loop control system based on the PPO algorithm are not solely dependent on direct coupling with the natural vortex shedding frequency but may also reflect a comprehensive optimization of overall flow field stability. The closed-loop control system may identify that high-frequency actuation suppress asymmetric vortices more effectively, and even if the reduced frequency does not match the natural vortex shedding frequency, it can still achieve favorable control performance.

While this study confirms the feasibility of reinforcement learning-based closed-loop plasma control, its scalability to larger aircraft and adaptability to varying environmental conditions remain unvalidated. Environmental factors such as atmospheric pressure, temperature, and high Reynolds number flow separation may affect flow control performance. Future research will prioritize algorithm refinement, experimental validation, and engineering integration. Optimization will improve adaptability across diverse conditions, expanded testing will evaluate robustness, and further refinements will enhance energy efficiency for practical application. These advancements aim to advance plasma flow control technology for high-angle-of-attack aircraft flight.

IV. Summary and conclusion

This study introduces three asymmetric vortex control strategies: vortex interaction regulation, flow field stability optimization, and velocity gradient control based on vortex stability theory. These strategies guided the design of a three-electrode DBD plasma actuator, aimed at enhancing vortex stability and minimizing lateral force. Optimal actuation parameters were obtained through PPO-based closed-loop control in an open-return wind tunnel and validated in a low-speed closed-return wind tunnel. Experimental results from synchronized pressure and PIV measurements show that closed-loop control improves vortex stability, reduces the total lateral force coefficient by 68.5%, and decreases energy consumption by 70% compared to steady plasma actuation. Furthermore, stability analysis of stationary points confirms that optimized control parameters enhance vortex symmetry and suppress flow disturbances. Compared to traditional open-loop control, this reinforcement learning-based approach increases adaptability, reduces dependence on predefined parameters, and improves control accuracy. These findings provide technical guidance for developing intelligent plasma control systems to enhance aircraft stability, maneuverability, and flight performance at high angles of attack. Future research will focus on high-Reynolds-number validation, energy efficiency optimization, and extending closed-loop control to practical aerodynamic configurations, paving the way for miniaturized, intelligent, and tailless aerodynamic control systems.

Acknowledgements

Project supported by the National Natural Science Foundation of China (No.52350072) and the National Key Laboratory Foundation of China (No. 614220220200110).

Author Declarations

Conflict of Interest

The authors have no conflicts to disclose

Data availability

The data that support the findings of this study are available from the corresponding authors upon reasonable request

References

[1] Keener, E. R., and Chapman, G. T., “Similarity in vortex asymmetries over slender bodies and wings,” AIAA Journal, 15 (9), 1370-1372 (1977).

[2] Shahriar, A., Kumar, R., and Shoele, K., “Vortex dynamics of axisymmetric cones at high angles of attack,” Theoretical and Computational Fluid Dynamics, 37 (5), 337-356 (2023).

[3] Zilliac, G. G., Degani, D., and Tobak, M., “Asymmetric vortices on a slender body of revolution,” AIAA Journal, 29 (5), 667-675 (1991).

[4] Deng, X. Y., Wang, Y. K., “Asymmetric vortices flow over slender body and its active control at high angle of attack,” Acta Mechanica Sinica, 20 (6), 567-579 (2004).

[5] Cai, J., Liu, F., and Luo, S., “Stability of symmetric vortices in two-dimensions and over three-dimensional slender conical bodies,” Journal of Fluid Mechanics, 480 (4), 65-94 (2003).

[6] Zhai, J., Zhang, W. W., and Wang, H. L., “Reviews of forebody vortex control method at high

angles of attack," Acta Aerodynamica Sinica, 35 (3), 354-367 (2017).

[7] Ma, B., Deng, X., and Chen, Y., "Effects of forced asymmetric transition on vortex asymmetry around slender bodies," AIAA Journal, 45 (11), 2671-2676 (2007).

[8] Chen, X. R., Deng, X. Y., and Wang, Y. K., "Influence of nose perturbations on behaviors of asymmetric vortices over slender body," Acta Mechanica Sinica, 18 (6), 581-593 (2002).

[9] Choi, J., Jeon, W., and Choi, H., "Mechanism of drag reduction by dimples on a sphere," Physics of Fluids, 18 (4), 041702 (2006).

[10] Sirangu, V., and Terry, N. G. T.,"Flow control of a slender blunt-nose body at high angles of attack," Journal of Aircraft, 49 (6), 1904-1912 (2012).

[11] Lopera, J., Terry, N. G. T., and Patel, M. P., "Forebody geometry effects on the flow of a blunt-nose projectile at high alpha," Journal of Aircraft, 44 (6), 1906-1922 (2007).

[12] Zhang, W., Liu, X., and Zhai, J., "Experimental study on side force alleviation of conical forebody with a fluttering flag," Physics of Fluids, 24 (12), 124105 (2012).

[13] Deng, X. Y., Tian, W., and Ma, B. F., "Recent progress on the study of asymmetric vortex flow over slender bodies," Acta Mechanica Sinica, 24 (5), 475-487 (2008).

[14] Luo, Z. B., and Xia, Z. X., "Advances in synthetic jet technology and applications in flow control," Advances in Mechanics, 35 (2), 221-234 (2005).

[15] Leu, T., Chang, J., and Lu, P., "Experimental investigation of side force control on cone-cylinder slender bodies with flexible micro balloon actuators," Experimental Thermal & Fluid Science, 29 (8), 909-918 (2005).

[16] Zheng, B. R., Lin, D. L., Jin, Y. Z., Qi, S.J., Hu, Y. Z., Chen, Q. L., and Bian, D. L., "Turbulent skin-friction drag reduction by annular DBD plasma synthetic jet actuator," Physics of Fluids, 35 (12), 125-129 (2023).

[17] Maslov, A. A., Zanin, B. Y., and Sidorenko, A. A., "Plasma control of separated flow asymmetry on a cone at high angles of attack," Proceedings of the 42th Aerospace Sciences Meeting and Exhibit, Reno, NV, U.S.A., AIAA-2004-0843.

[18] Liu, F., Luo, S. J., Gao, C., Meng, X. S., Hao, J. N., Wang, J. L., and Zhao, Z. J., "Flow control over a conical forebody using duty-cycled plasma actuators," AIAA Journal, 46 (11), 2969-2973 (2008).

[19] Zheng, B. R., Gao, C., Li, Y. B., Liu, F., and Luo, S. J., "Flow control over a conical forebody by periodic pulsed plasma actuation," Plasma Science and Technology, 15 (4), 350-356 (2013).

[20] Long, Y. X., Li, H. X., Meng, X. S., and Hu, H. Y., "Optimized plasma actuation on asymmetric vortex over a slender body," Applied Physics Letters, 112 (1), 014101 (2018).

[21] Meng, X. S., Long,Y. X., Wang, J. L., Liu, F., and Luo, S. J., "Dynamics and control of the vortex flow behind a slender conical forebody by a pair of plasma actuators," Physics of Fluids, 30 (2), 024101 (2018).

[22] Hui, W. W., Meng, X. S., Li, H. X., and Liu, F., "Flow induced by a pair of plasma actuators on a circular cylinder in still air under duty-cycle actuation," Physics of Fluids, 34 (12), 123613 (2022).

[23] Zheng, B. R., Xue, M., and Ge, C., "Forebody asymmetric vortex control with extended dielectric barrier discharge plasma actuators," Chinese Physics B, 29 (6), 064703 (2020).

[24] Zheng, B. R., Ke, X. Z., Ge, C., Zhu, Y. F., Wu, Y., Liu, F., and Luo, S. J., "Electrical and flow characteristics of a double-side sliding pulsed discharge plasma actuator," AIAA Journal, 58 (2), 733-746 (2020).

[25] Liu, F., Luo, S. J., Gao, C., and Meng, X. S., "Plasma actuators for aerodynamic flow control: Recent advances and challenges," AIAA Journal, 59(3), 1081-1092 (2021).

[26] Wang, J., Zhang, H., and Lee, S., "Active and passive vortex control techniques for aircraft stability enhancement at high angles of attack," Aerospace Science and Technology, 118, 107226 (2022)

[27] Cai, J., Luo, S., and Liu, F., "Stability of symmetric and asymmetric vortices over slender conical wing-body combinations," AIAA Journal, 44 (7), 1601-1608 (2006).

[28] Cai, J. S., Tsai, H-M., Luo, S. J., and Liu, F., "Stability of vortex pairs over slender conical bodies: analysis and numerical computation," AIAA Journal, 46 (3), 712-722 (2008).

[29] Zheng, B. R., Gao, C., Li, Y. B., Liu, F., and Luo, S. J., "Flow control over a conical forebody by duty cycle actuations," Plasma Science and Technology, 14 (1), 58-63 (2012).

[30] Zheng, B. R., Gao, C., Li, Y. B., Liu, F., and Luo, S. J., "Flow control over a conical forebody by periodic pulsed actuation," Plasma Science and Technology, 15 (4), 350-356 (2013).

[31] Brunton, S. L., Noack, B. R., Koumoutsakos, P., "Machine Learning for Fluid Mechanics," Annual Review of Fluid Mechanics, 52, 477-508 (2020).

[32] Vinuesa, R., Brunton, S. L., McKeon, B. J., "The transformative potential of machine learning for experiments in fluid mechanics," Nature Reviews Physics, 5, 536-545 (2023).

[33] Mnih, V., Kavukcuoglu, K., Silver, D., Rusu, A. A., Veness, J., Bellemare, M. G., Graves, A., Riedmiller, M., Fidjeland, A. K., Ostrovski, G., Petersen, S., Beattie, C., Sadik, A., Antonoglou, I., King, H., Kumaran, D., Wierstra, D., Legg, S., Hassabis, D., "Human-level control through deep reinforcement learning, " *Nature*, 518, 529-533 (2015).

[34] Shimomura, S., Sekimoto, S., Oyama, A., Fujii, K., Nishida, H., "Closed-loop flow separation control using the deep Q-network over airfoil," AIAA Journal, 58(1), 4260-4270 (2022).

[35] Lillicrap, T. P., Hunt, J. J., Pritzel, A., Heess, N., Erez, T., Tassa, Y., Silver, D., Wierstra, D., "Continuous control with deep reinforcement learning," Computer Science, 2015(10), 67722-4 (2015).

[36] Zhang, S., Zhang, C, "Trust region policy optimization via entropy regularization for reinforcement learning," *Neurocomputing*, 518, 529-533 (2024).

[37] Chen, J., Zong, H. H., Song, H. M., Wu, Y., Ling, H., Su, Z., "Closed-loop plasma flow control of a turbulent cylinder wake flow using machine learning at Reynolds number of 28,000," Physics of Fluids, 36(1) (2024).